PNAS Nexus, 2023, 2, 1–8
https://doi.org/10.1093/pnasnexus/pgad177
Advance access publication 31 May 2023
Research Report

Hyper-anti-freezing bionic functional surface to −90°C

Zhaolong Wang[a,*], Mingzhu Xie[a], Qing Guo[b], Yibo Liao[a], Ce Zhang[c], Yongping Chen[d,e,*], Zhichao Dong[f,*] and Huigao Duan[a,*]

[a]Interdisciplinary Research Center of Low-carbon Technology and Equipment, College of Mechanical and Vehicle Engineering, Hunan University, 1 South Lushan, Changsha 410082, PR China
[b]MOE Key Laboratory for Power Machinery and Engineering, School of Mechanical and Power Engineering, Shanghai Jiao Tong University, 800 Dongchuan Road, Shanghai 200240, PR China
[c]Qian Xuesen Laboratory of Space Technology, China Academy of Space Technology (CAST), 104 Youyi Road, Beijing 100094, PR China
[d]Key Laboratory of Energy Thermal Conversion and Control of Ministry of Education, School of Energy and Environment, Southeast University, 2 Sipailou Road, Nanjing 210096, PR China
[e]Jiangsu Key Laboratory of Micro and Nano Heat Fluid Flow Technology and Energy Application, School of Environmental Science and Engineering, 99 Xuefu Road, Suzhou University of Science and Technology; Suzhou, Jiangsu 215009, PR China
[f]Chinese Academy of Sciences Key Laboratory of Bio-inspired Materials and Interface Sciences, Technical Institute of Physics and Chemistry, Chinese Academy of Sciences, 1 Hudong Road, Beijing 100190, PR China
*To whom correspondence should be addressed: Email: zhaolongwang@hnu.edu.cn (Z.W.); ypchen@seu.edu.cn (Y.C.); dongzhichao@mail.ipc.ac.cn (Z.D.); duanhg@hnu.edu.cn (H.D.)
Edited By: Cristina Amon

Abstract

Freezing phenomenon has troubled people for centuries, and efforts have been made to lower the liquid freezing temperature, raise the surface temperature, or mechanical deicing. Inspired by the elytra of beetle, we demonstrate a novel functional surface for directional penetration of liquid to reduce icing. The bionic functional surface is fabricated by projection microstereolithography (PμSL) based three dimensional printing technique with the wettability on its two sides tailored by TiO_2 nanoparticle sizing agent. A water droplet penetrates from the hydrophobic side to the superhydrophilic side of such a bionic functional surface within 20 ms, but it is blocked in the opposite direction. Most significantly, the penetration time of a water droplet through such a bionic functional surface is much shorter than the freezing time on it, even though the temperature is as low as −90°C. This work opens a gate for the development of functional devices for liquid collection, condensation, especially for hyperantifogging/freezing.

Keywords: anti-icing, PμSL based 3D printing, liquid unidirectional penetration, Laplace force

Significance Statement

Although various projects apply different mechanisms for anti-icing, such as thermal deicing, mechanical deicing, and sprinkling salt, those ways waste a lot of energy and cost too much. The elytra of beetle with different wettability on its two sides and unique porous structures enable ultrafast water penetration from its hydrophobic side to superhydrophilic side. Our biomimetic functional surfaces demonstrate marvelous performance of anti-icing because the penetration time of a water droplet through them is much shorter than the freezing time even at −90°C. Our bionic functional surfaces pave a novel way for the development of functional devices for liquid collection, condensation, especially for hyperantifogging/freezing.

Introduction

In nature, water becomes ice at subzero temperature within 100 s (1, 2), and such a phenomenon brings us a lot of inconvenience and disasters in the past thousands of years (3–5). After hundreds of years' study, anti-icing can be achieved in passive and active ways (6) to inhibit ice nucleation, hinder ice crystal growth, and reduce ice adhesion, as well as water removal before icing (7). Typical passive anti-icing is ambiguous (8), including slippery surfaces with low energy of adhesion (9, 10) and an ultralow ice nucleation temperature (11), as well as droplets bouncing away below the freezing point (12). Among them, slippery surfaces are achieved based on the microstructures or the surfaces themselves which contribute to the easy removal of liquid/ice, including superhydrophobic surfaces to reduce the adhesion of liquid (13–15), icephobic surfaces for easy removal of the ice (16, 17), etc. Active anti-icing is induced by an external stimulus that induces magnetism (18, 19), optothermal (20, 21), and electric heating (22, 23) that raise the temperature of these surfaces for preventing icing and melting the existing ice by using much energy.

In nature, plants and animals have evolved over millions of years in a natural way that is not only faultlessly adapted to nature but also close to perfection. Scientists attempt to model the function of plants and animals in terms of characteristic and

Competing Interest: The authors declare no competing financial interest.
Received: February 20, 2023. **Revised:** May 10, 2023. **Accepted:** May 18, 2023
© The Author(s) 2023. Published by Oxford University Press on behalf of National Academy of Sciences. This is an Open Access article distributed under the terms of the Creative Commons Attribution-NonCommercial-NoDerivs licence (https://creativecommons.org/licenses/by-nc-nd/4.0/), which permits non-commercial reproduction and distribution of the work, in any medium, provided the original work is not altered or transformed in any way, and that the work is properly cited. For commercial re-use, please contact journals.permissions@oup.com

advancing designs, creative thinking and understanding of the principles of various physical processes that provide a bridge between biology and technology, which help us to solve technical problems (24, 25). By reproducing the principles of biology with advancing means, people will not only break through existing bottlenecks but also perfectly solve the technical problems at the same time. Generally, bionic superhydrophobic surfaces (i.e. water contact angle (CA) >150° and sliding angle less than 10°) inspired by lotus leaf (26–28), butterfly wing (29, 30), and antarctic scallop (31) are commonly used in those anti-icing phenomena (32).

Inspired by the elytra of beetle, we herein propose a uniquely mimicked functional membrane with numerous microholes. The bionic porous membrane was manufactured by the projection microstereolithography (PμSL) based three dimensional (3D) printing technique (33–36) precisely. One surface of the bionic porous membrane exhibited superhydrophilicity treated with TiO_2 nanoparticle sizing agent, while the other original surface was hydrophilic that induced the different Laplace pressures. Hence, the bionic porous membrane with asymmetric wettability enables the unique unidirectional microfluidic performance. Most significantly, liquid can penetrate the bionic porous membrane before icing that enables passive anti-icing even at −90°C. The proposed 3D printed bionic porous membrane promise applications in water resistible and breathable equipment (37, 38), ant-icing devices (13, 39), etc.

Results

Design and fabrication of the bionic functional surfaces

There are numerous through microchannels with arbitrary cross-sectional shapes on the elytra of beetle for gas exchange and unidirectional transportation of water (Fig. 1A). Notably, the CAs of the inner and outer surfaces with those through microchannels of elytra of beetle are different (Online Supplementary Appendix, Fig. S1), which partially contribute to the survival of beetle in a cold and humid environment (40) (Figs. 1A–C). Our functional surfaces are inspired by the unique microsturctures and properties of beetle's elytra. A porous membrane with a pore length of 400 μm, interlaced by 200 μm cylinders, was precisely fabricated by PμSL based 3D printing technique (Online Supplementary Appendix, Figs. S2 and S3, Table S1 and Method). The bionic functional porous membrane (Fig. 1D) enables the ultrafast unidirectional penetration of a water droplet at an extremely low temperature as low as −90°C (Fig. 1E), instead of freezing on a porous membrane without any treatment (normal surface) within several seconds (Fig. 1F).

The TiO_2 nanoparticle sizing agent ($TiO_2/H_2O = 1/5$ w/w) was dripped onto one side of the porous membrane to manipulate the wettability of it after the 3D printing process (Online Supplementary Appendix, Fig. S4). The CA of a printed flat surface is around 60° (Materials and Method). In addition, the superhydrophobic membrane is much smoother than the one without any treatment, whose total thickness is 500 μm, as observed from their scanning electron microscope (SEM) figures. The bionic functional surface (Online Supplementary Appendix, Fig. S5) consists of a superhydrophilic surface (CA = 8°) and a hydrophobic surface (CA = 107°, Online Supplementary Appendix, Fig. S6) with microholes in-between. The advancing CA of a printed bionic functional surface treated with TiO_2 slurry is decreased to 14°, while the advancing CA of a printed surface with same regularly arranged microholes is increased to around 98° (Online Supplementary Appendix, Fig. S7).

Discussion

Unidirectional fluidic performance for bionic functional surfaces

The unidirectional microfluidic performance of our bionic functional surfaces is schematically shown in Fig. 2A, during which the capillary force formed by the meniscus of liquid in the microholes within the bionic functional surface plays a crucial role. At the beginning, a deionized (DI) water droplet goes inside of the microholes because of the meniscus of liquid facing downward (Fig. 2A-i). Then, the capillary force accelerates the DI water passing through the microholes (Figs. 2B and C). However, the Laplace force dominates the further movement of the DI water upon reaching the upper openings of those microholes inside of the bionic functional surface (Online Supplementary Appendix, Fig. S8),

$$\Delta p = \frac{4\gamma \sin(\theta + \alpha)}{D} \tag{1}$$

where γ is the surface tension of the liquid, and D is the diameter of the microholes. θ is the static CA between a printed surface and a liquid droplet, and α is indicated in Fig. 2B. In addition, the maximum Laplace pressure appears when θ reaches the advancing CA (θ_a) of the bionic functional surface (41),

$$\Delta p_{\max} = \frac{4\gamma \sin\theta_a}{D} \tag{2}$$

The θ_a of a superhydrophilic surface is around 14°, leading to a fact that the Laplace force is not large enough to decrease the velocity of the water to 0 before reaching its maximum value because of the inertia of the water (Fig. 2A-ii and B). Then, the water will come out from the openings on the superhydrophilic surface (Fig. 2D, Online Supplementary Appendix, Fig. S9 and Movie S1). In contrast, the DI water also comes into microholes from the superhydrophilic surface, reaching the bottom openings with a relatively high velocity. Similarly, the backward Laplace force decreases the velocity of the water gradually. Different from the situation on the superhydrophilic surface, the Laplace pressure is large enough to decrease the velocity of the water to 0 before the θ reaching the θ_a (Fig. 2A-ii). At last, the water will be forbidden to pass through the bionic functional surface when the water droplet is dropped on the superhydrophilic surface (Fig. 2E, Online Supplementary Appendix, Fig. S10 and Movie S2). Moreover, the unidirectional penetration of water cannot be achieved with a superhydrophobic/superhydrophilic CA pair, a hydrophobic/superhydrophobic CA pair, or a hydrophobic/hydrophobic one (Online Supplementary Appendix, Figs. S11 and S12 and Movies S3–S5).

The size of the droplet makes a difference in its CA (Online Supplementary Appendix, Fig. S13), and the CA reaches the maximum when the width of the microholes is 600 μm with a 2 μl droplet. Similarly, the size of the microholes also greatly influences the CA of the membrane, and the maximum CA appears when the width of microholes is 600 μm (Online Supplementary Appendix, Fig. S14). The theoretical Laplace pressure difference (Δp) on the two sides of a bionic functional surface decreases with the increase of the microhole's size (Fig. 2F), leading to a fact that the penetration time of a water droplet passing through a bionic functional surface decreases with the increase of the microhole's size (Fig. 2G, Online Supplementary Appendix, Fig. S15 and Movie S6). In addition, the size of water droplets (Online Supplementary Appendix, Fig. S16), the length of the microholes covered with TiO_2 nanoparticles (Online Supplementary Appendix, Fig. S17), and the surface tension of the liquid (Online Supplementary

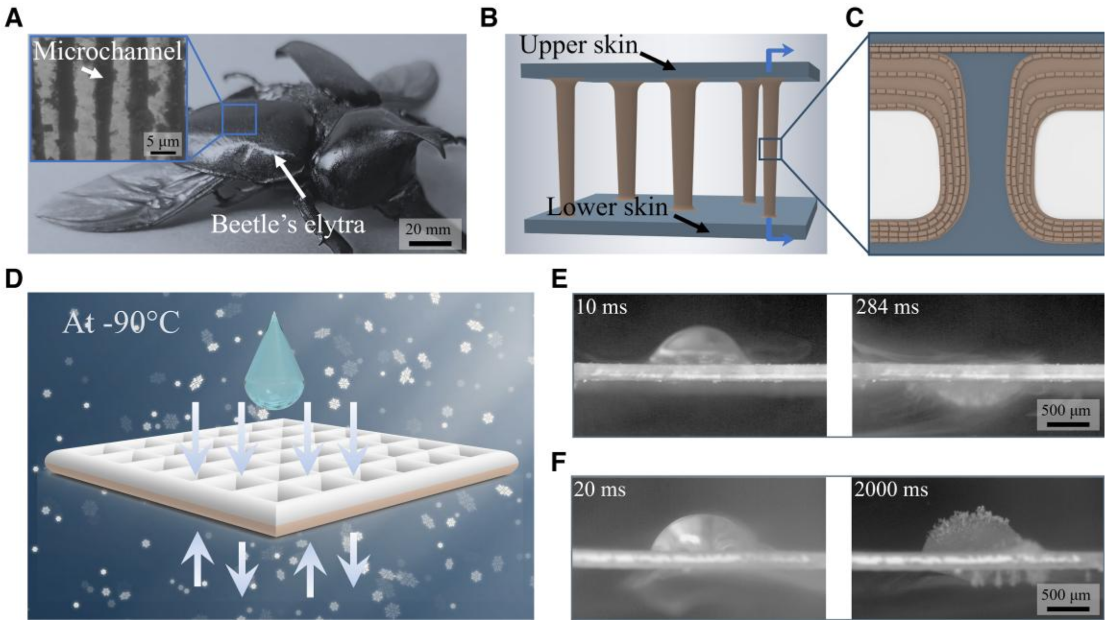

Fig. 1. A 3D printed bionic functional surface. A) Beetle. B) Beetles' elytron microstructures. C) Cross-sectional view of beetle's elytron. D) Schematic diagram of a bionic functional surface. E) The penetration process of a water droplet through the bionic functional surface at −90°C. F) A water droplet will freeze on a printed flat surface without any treatment within 2000 ms at −90°C.

Appendix, Figs. S18 and S19 and Movies S7 and S8) also make a big difference on the unidirectional microfluidic performance of our bionic functional surfaces. However, it should be pointed out that a bionic functional surface with large microholes might fail if ethyl alcohol is used as the working fluid because of its low adhesion force significantly affects the Laplace pressure at the openings of the microholes (Online Supplementary Appendix, Fig. S20 and Movie S9).

Lattice Boltzmann method simulation of the unidirectional water transportation through bionic functional surfaces

The unidirectional transport of water through bionic functional surfaces is found to be conditional by numerical calculations (Online Supplementary Appendix, Fig. S21 and Method). For the hydrophilic/superhydrophilic CA pair, successful unidirectional penetration of water droplets is found only when the bionic functional surface is placed upward, i.e. the water droplet is transported from the hydrophilic side to the superhydrophilic side (Fig. 3A and B; Online Supplementary Movies S10 and S11). However, when the water droplet is placed on a bionic functional surface with superhydrophilic CA pair, it penetrates through the bionic functional surface from both directions (Fig. 3C and D; Online Supplementary Appendix, Figs. S22 and S23).

To look into the physics further, we propose a thermodynamic free energy model to calculate the capillary pressure along the penetration direction inside microholes on the bionic functional surface. For a bionic functional surface made of a single layer membrane with rectangular microholes and circular-shaped solid cross-section (Online Supplementary Appendix, Fig. S24 and Method), the local capillary force $P_{cap}(x) = \frac{dE}{dV}$ (42), which is the change in surface energy per volume, is calculated in permeation direction x with the consideration of meniscus shape. $P_{cap}(x)$ shares a similar trend of first increasing (due to flow channel geometry) and then decreasing (due to superhydrophilicity at the bottom surface) pattern with respect to x in all cases. The more hydrophilic θ_t is, the larger range of x where $P_{cap}(x)$ is negative, indicating that it is thermodynamically preferred for the liquid–vapor interface to keep moving in x direction (Fig. 3E).

When θ_t is hydrophobic (blue lines), $P_{cap}(x) = 0$ occurs at much smaller x than hydrophilic θ_t, which explains the no-penetration behaviors on such surfaces due to lack of penetration propulsion. The drop in $P_{cap}(x)$ is caused by the sudden change in intrinsic CA from θ_t to θ_b. With $h_{b/t}$ being smaller, the sudden decrease in $P_{cap}(x)$ occurs earlier (Fig. 3F). In current settings, $P_{cap}(x)$ is always negative as long as $h_{b/t} < 70\%$, and its average value is decreasing with the decrease of $h_{b/t}$, suggesting large penetration rate rising from great capillary pressure. Similarly, we find that the absolute value of capillary pressure is larger at smaller d_a, showing a greater capillary wicking effect to propel liquid penetration (Fig. 3G). However, it is worth noting that, ultrasmall d_a will also bring large flow resistance (not incorporated in capillary pressure model), resulting in a nonmonotonic effect on penetration rate.

The hyperantifreezing characteristics of our bionic functional surfaces

The freezing time of a 2 μL DI water droplet on a printed flat surface made of the same material and roughness is tens of seconds (Fig. 4A), which decreases with the decrease of the temperature (Fig. 4B, and Online Supplementary Appendix, Fig. S25). In contrast, a 2 μL water droplet penetrates the bionic functional surface within 96 ms when the surrounding temperature is above −30°C (Figs. 4A, C, and D; Online Supplementary Movies S12 and S13), and the water droplet is not frozen, while a water droplet on a similar membrane without CA difference is frozen around 18 s at −30°C (Online Supplementary Appendix, Fig. S26). The penetration speed of a water droplet decreases with the decrease of the surrounding temperatures (Fig. 4C–G) because the surface tension of water decreases with the decrease of the surrounding temperatures (43), which reduces the Laplace force at the openings of the superhydrophilic surface. But the time of a water droplet passing through the bionic functional surface is still shorter than the freezing time of

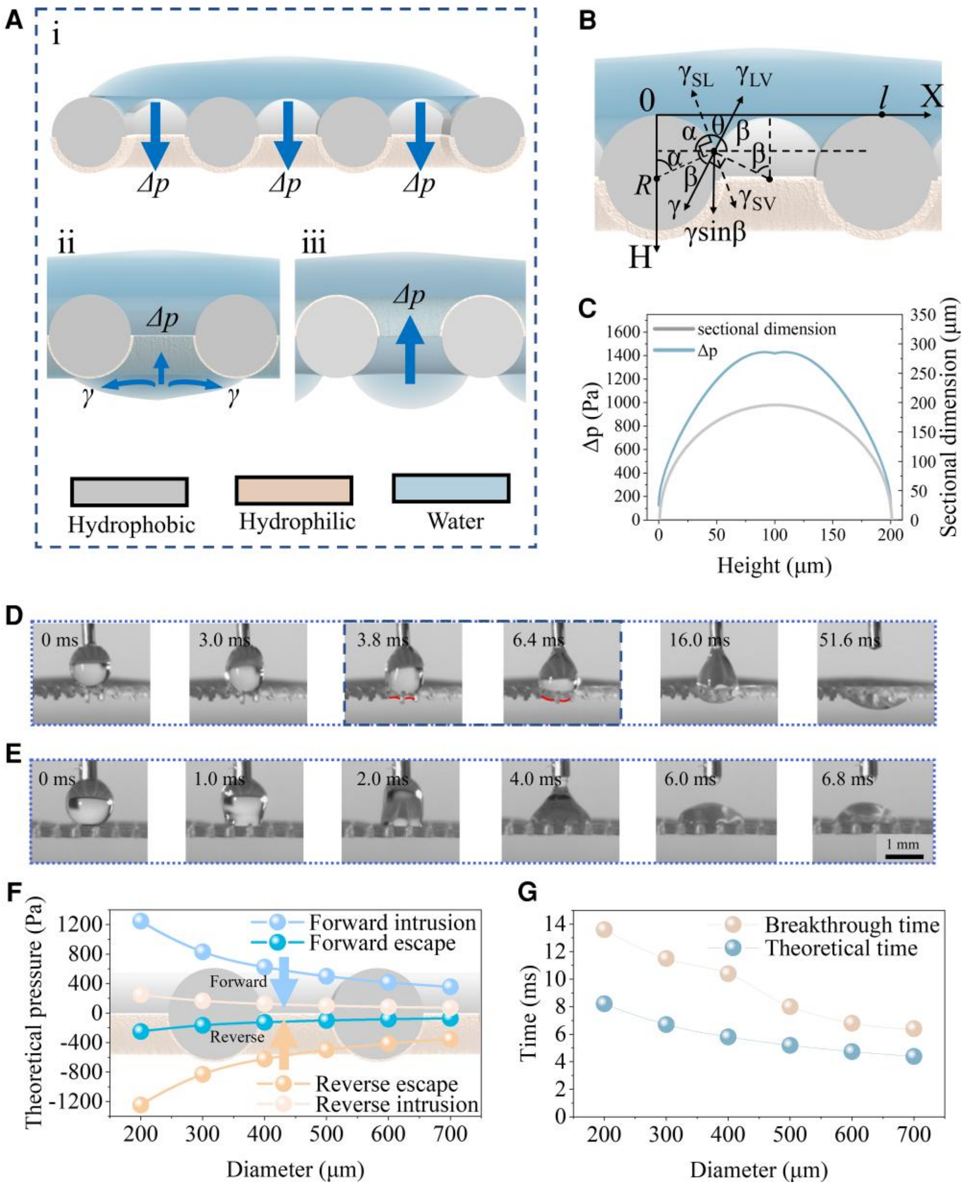

Fig. 2. The ultrafast unidirectional penetration of water through a bionic functional surface. A) Schematic of unidirectional liquid penetration performance of a bionic functional surface. B) Capillary rise of water inside of a microhole. C) Capillary force inside a microhole. D) A droplet penetrates the bionic functional surface from the hydrophobic side to the superhydrophilic side. E) A water droplet is blocked on the superhydrophilic surface. F) Laplace pressure on the two sides of the bionic functional surface. G) The influence of membrane apertures on the penetration time through the bionic functional surface.

the water on it, leading to a fact that the water droplet will not be frozen on such a bionic functional surface even at −90°C (Figs. 4C–E). In contrast, a small part of water is frozen on the hydrophobic side during the penetration process at −95°C (Movie S14) because the water droplet starts to freeze at the interface of the water droplet and the bionic functional surface before passing through it, which slows down the penetration of the water passing through it. The quite high surface tension of a water droplet increases the penetration time longer than its freezing time on the hydrophobic side at −120°C, the water droplet is frozen to ice before penetrating the bionic functional surface (Fig. 4G).

Conclusion

In conclusion, the near-to-zero Laplace force on the superhydrophilic side of a bionic functional surface (the other side is hydrophobic) with regularly arranged microholes enabled the ultrafast unidirectional penetration of a water droplet from its hydrophobic side to superhydrophilic side within 15 ms, which is shorter than the freezing time of a water droplet on such a bionic functional surface if the temperature is not lower than −90°C. Our bionic functional surface paves a new way for designing hyperantifreezing functional surfaces and liquid diode.

Materials and methods

Fabrication of the membrane with PμSL-based 3D printing technique

A 3D membrane was firstly modeled with a software, then it was sliced into several hundred 2D photos. A 3D printer (BMF-P140, China, Shenzhen), which is based on a kind of the surface

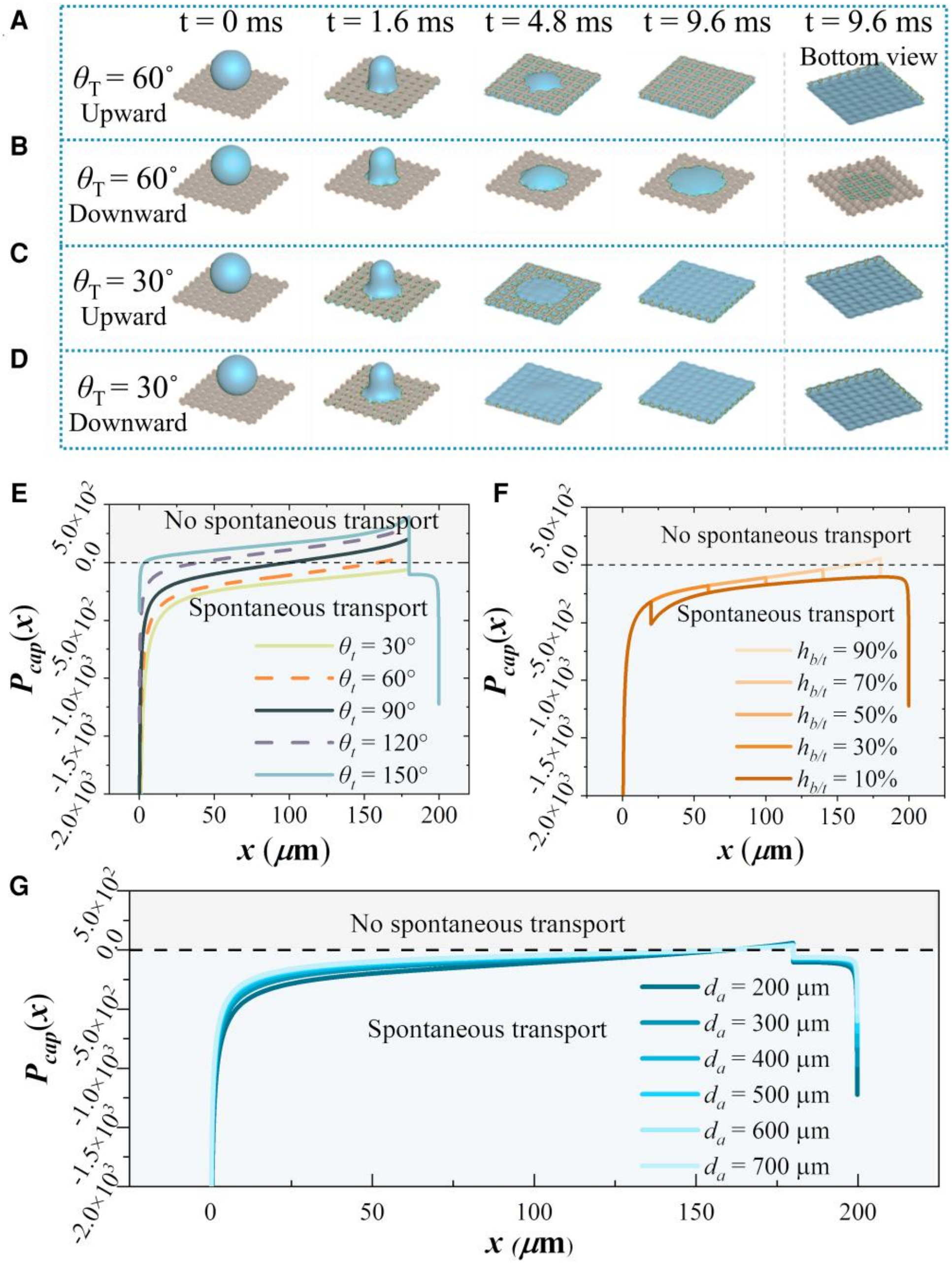

Fig. 3. Lattice Boltzmann method simulation of the unidirectional water transportation through a bionic functional surface. A) Dynamic process of a droplet permeating on hydrophilic side of a bionic functional surface with $\theta_t = 60°$ (facing upward). B) Dynamic process of a droplet permeating on hydrophilic side of a bionic functional surface with $\theta_t = 60°$ (facing downward). C) Dynamic process of a droplet permeating on superhydrophilic side of a bionic functional surface with $\theta_t = 30°$ (facing upward). D) Dynamic process of a droplet permeating on superhydrophilic side of a bionic functional surface with $\theta_t = 30°$ (facing downward). E) Effect of θ_t on capillary pressure. F) The effect of $h_{b/t}$ on capillary pressure. G) The effect of microholes on capillary pressure.

projection light curing 3D printed technology (44), is appropriately applied for fabricating 3D complicated microstructures with high resolution, high precision, cross-scale processing, high processing efficiency, wide applicable materials, as well as low processing cost. The membranes were removed lightly from the tablet after the printing process, and soaked in ethanol for 1 min to wash out the photosensitive resin on them.

Preparation of TiO_2 nanoparticle slurry

An appreciable amount of TiO_2 nanoparticle powder (98% metals basis, ≤100 nm), which was purchased from Aladdin, was added to a beaker filled with water so that the ratio of TiO_2 to water was 1:5. Finally, we stirred it evenly.

Fabrication of the membrane with different CAs on its two sides

The TiO_2 nanoparticle sizing agent therewith spread on the dry porous membrane homogeneously. After simply utilizing absorbent paper to absorb the moisture and air-drying naturally for 24 h, one side of the membrane and the inside of the sheet was covered with TiO_2 nanoparticles at the end.

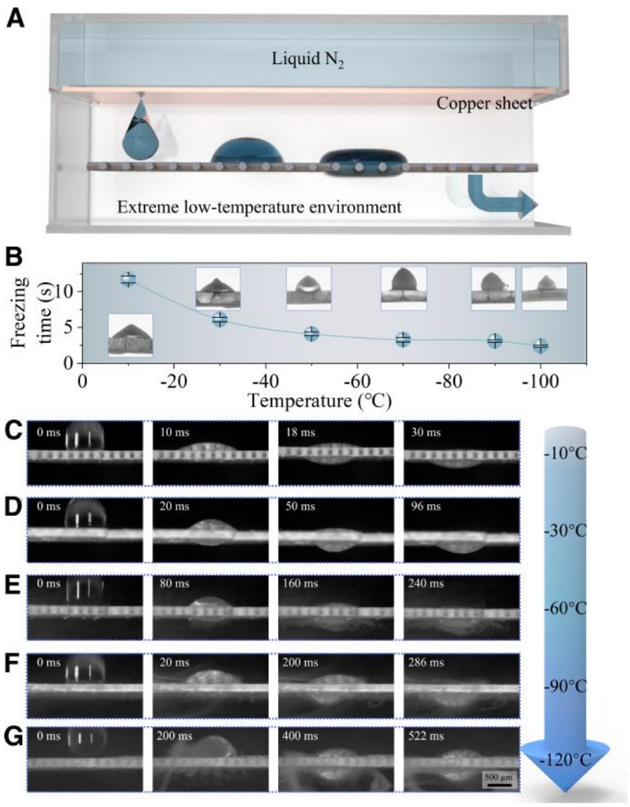

Fig. 4. The hyperantifreezing performance of a bionic functional surface. A) The schematic diagram of liquid unidirectional penetration on the bionic functional surfaces at extremely low temperatures. B) The influence of temperature on freezing time of a water droplet on a printed flat surface. C–G) The penetration process of a water droplet passing through a bionic functional membrane at −10, −30, −60, −90, and −120°C, respectively.

Test of wetting property

We first placed the porous membrane or tablet on the test platform of the contact angle measuring device (SDC-100, SINDIN Company). Afterwards, we dropped 2 µl water droplets ($\gamma_W = 72\ mN \cdot m^{-1}$) on the surface of the porous membrane or tablet, which were extruded from a syringe needle. Finally, the images that droplets contacted the surfaces were transmitted to a software, the diverse contact angles for different surfaces were obtained.

Liquid unidirectional penetration

Water droplet was provided by a microinjection located above a bionic functional surface. A water droplet was extruded through the needle by hand, then it contacted the hydrophobic side of the bionic functional surface, and finally penetrated to the superhydrophilic surface, which was regarded as the "forward direction" of the liquid unidirectional penetration. In contrast, if the bionic functional membrane turned around and the hydrophilic surface faced the needle, the first microdroplet jointly spread and grew up rather than penetrating to the other side, which was the "reverse direction" of the liquid unidirectional penetration.

The low-temperature experimental setups

By using a 3D printer (Kobra, Anycubic Company) based on fused deposition modeling technology, we designed and manufactured the low-temperature experiment setups (Online Supplementary Appendix, Fig. S27), including the base on which the bionic functional surface was placed, the tank for liquid N_2, and a copper sheet with 0.1 mm thickness in the middle between the base and the tank. The front side of the middle of the base is a gap for observation with a high-speed camera. The left side of the top of the tank is an entrance for filling liquid N_2, and the middle side of the top of it is a channel for inserting a syringe and dropping water droplets. The copper sheet, which is cut out with a hole in the center for dropping liquid droplets, is bonded to the bottom of the tank for better heat transfer.

Preparation of samples for low-temperature experiments

We firstly put bionic Janus functional surfaces into an oil bath (−100°C) for an hour to decrease the temperature of them. Meanwhile, we filled the tank with liquid N_2 to decrease the temperature of the whole setup. Then, the porous membrane was placed in the center of the base. Furthermore, the whole equipment was placed in a glovebox full of N_2.

Temperature measurement

We measured the temperature with a thermocouple temperature meter (Smart Sensor AS887, China), whose measuring head is put near the upper surface of bionic functional surface. The temperature was precisely controlled by the liquid N_2.

The injection of water droplets

A channel in the middle of liquid N_2 tank is reserved for the low-temperature experiments. We inserted the syringe with insulation into the channel quickly and kept the syringe 1 cm above the bionic functional membrane. A 2 µl water droplet would be extruded from the syringe to the upper surface of the bionic functional membrane.

Observation of antifreezing phenomenon of the printed liquid diode

A high-speed camera (HX-7 s, NAC Memrecam) was placed in front of the low-temperature experimental setup. When a water droplet was extruded from an injection, we used the high-speed camera to observe the process that the water droplets penetrated to the superhydrophilic side fleetly instead of frozen on the hydrophobic side through the reserved window. The water droplets could penetrate the bionic functional membrane one by one in a twinkling. By changing the temperature, the anti-icing performance of our bionic functional membrane was observed at different subzero temperatures from −10°C to −120°C.

Lattice Boltzmann method

The 3D single-component multiphase pseudopotential lattice Boltzmann method with Peng-Robinson equation of state (45) is employed to study droplet permeation dynamics on the bionic functional membranes. On-fourth of the computational domain, which is comprised of $80 \times 80 \times 140$ lattices, is simulated with symmetrical boundaries. The droplet is initialized in its own saturated vapor where the lower liquid–vapor interface of the droplet just contacts with the bionic functional membrane, and let deform spontaneously in isothermal environment at $T = 0.85T_c$ under the simultaneous effects of capillary force and gravitational force. Unit conversions are done with $\Delta x = l_{c,real}/l_{c,LB}$ and $\Delta t = t_{c,real}/t_{c,LB}$, where $l_c = \sqrt{\sigma/(\Delta\rho g)}$ and $t_c = \sqrt{l_c/g}$ are the capillary length and characteristic time scale, respectively. The default parameters for numerical cases are $Lx \times Ly \times Lz = 1.6\ mm \times 1.6\ mm \times$

2.8 mm, droplet diameter $d_p = 1.5$ mm, the cross-sectional diameter $d_c = 200$ μm, the membrane aperture $d_a = 200$ μm, CA at the top surface $\theta_t = 60°$, CA at the bottom surface $\theta_b = 3°$ and their height ratio $h_{b/t} = 10\%$. With the abovementioned parameters, the typical Bond number $Bo = \Delta\rho g d_p^2/(4\sigma) = 0.061$, suggesting the surface tension is dominant during the permeation process. Additionally, the Weber number can be determined by $We = \rho v^2 l/\sigma = 5.556 \times 10^{-4}$, the Reynolds number can be determined by $Re = \rho v l/\mu = 4$, the capillary number can be determined by $Ca = We/Re = 1.389 \times 10^{-4}$.

Theoretical permeation model

The droplet permeation problem is simplified as a liquid–vapor interface sweeping from a repeating unit cell (i.e. a rectangular-shaped aperture formed by cylindrical rods). The shape of liquid–vapor interface at x direction is assumed to be spherical with an equivalent diameter $d = d_a + d_c - 2y$ and a local CA $\theta = \theta_t$ when $x < h_{b/t} d_c$, $\theta = \theta_b$ when $x \geq h_{b/t} d_c$. For the liquid–vapor interface to move to a distance of dx in x direction, a liquid–solid interface $A_{ls} = 4 l_{arc}(d_a + d_c - 2y - dy)$ is created where l_{arc} is the arc length shown by red solid line in the Online Supplementary Appendix, Fig. S24, and vapor–solid interface $A_{vs} = A_{ls}$ is destroyed. The change in liquid–vapor interfacial area is given by

$$A_{vl} = 2\pi\left[\left(\frac{1-\cos\alpha'}{\sin^2\alpha'}\right)\left(\frac{d_a + d_c - 2y - 2dy}{2}\right)^2 - \left(\frac{1-\cos\alpha}{\sin^2\alpha}\right)\left(\frac{d_a + d_c - 2y}{2}\right)^2\right] \tag{3}$$

where α and α' are angles of spherical caps at x and $x + dx$, respectively.

The total interfacial energy changes dE from (x) to $(x + dx)$ reads

$$dE = -\gamma_{vs} A_{vs} + \gamma_{ls} A_{ls} + \gamma_{vl} A_{vl} \tag{4}$$

The volume change between two meniscuses dV is estimated as

$$dV = 2\pi\left[\left(\frac{1-\cos\alpha_{ave}}{\sin^2\alpha_{ave}}\right)\left(\frac{d_a + d_c - 2y - dy}{2}\right)^2\right]dx \tag{5}$$

where α_{ave} is the average angle of α and α'.

$P_{cap}(x)$ is calculated as the surface energy over the volume change when the interface moves to a distance of dx in the permeation direction. With Young's equation $(\cos\theta = (\gamma_{vs} - \gamma_{ls})/\gamma_{vl})$,

$$P_{cap}(x) = \frac{dE}{dV} = \gamma_{vl}\frac{-A_{ls}\cos\theta + A_{vl}}{2\pi\left[\left(\frac{1-\cos\alpha_{ave}}{\sin^2\alpha_{ave}}\right)\left(\frac{d_a + d_c - 2y - dy}{2}\right)^2\right]dx} \tag{6}$$

where y, dy, α_{ave} can be obtained from geometrical relations.

Thus, according to minimal free energy principle, a negative value of $P_{cap}(x)$ indicates that it is thermodynamically favorable for liquid–vapor interface to move and permeate along x direction, and a positive $P_{cap}(x)$ means that the liquid–vapor interface is unlikely to permeate spontaneously.

Other characterization

The porous membranes were characterized by a microscope (MJ31, Mshot). Then we gilded the surfaces of porous membranes, and examined the surface morphology on the porous membrane by an SEM.

Supplementary material

Supplementary material is available at *PNAS Nexus* online.

Funding

This work was supported by the National Natural Science Foundation of China (52006056), and the Key-Area Research and Development Program of Guangdong Province (2020B090923003). The project was also supported in part by Natural Science Foundation of Hunan through Grant No. 2020JJ3012.

Author contributions

M.X., Y.L., H.D., and Z.W. conceived the project, carried out the experimental work, analyzed the data and wrote the manuscript. Q.G. provides methodology and investigation. Z.W., Y.C., and Z.D. supervised the whole project. All the authors discussed the results and commented on the manuscript.

Data availability

All study data are included in the article and Online Supplementary Appendix.

References

1 Bai GY, Gao D, Liu Z, Zhou X, Wang JJ. 2019. Probing the critical nucleus size for ice formation with graphene oxide nanosheets. *Nature*. 576:437–441.
2 Ubbelohde AR. 1964. Melting and freezing. *Nature*. 204: 1046–1049.
3 Ma RZ, *et al.* 2020. Atomic imaging of the edge structure and growth of a two-dimensional hexagonal ice. *Nature*. 577:60–63.
4 Marcott SA, *et al.* 2011. Ice-shelf collapse from subsurface warming as a trigger for Heinrich events. *P Natl Acad Sci USA*. 108: 13415–13419.
5 Yoda T, Miyaki H, Saito T. 2021. Freeze concentrated apple juice maintains its flavor. *Sci Rep*. 11:12679.
6 Kreder MJ, Alvarenga J, Kim P, Aizenberg J. 2016. Design of anti-icing surfaces: smooth, textured or slippery? *Nat Rev Mater*. 1(1):15003.
7 Ma LQ, Zhang ZC, Gao LY, Hu H. 2020. An exploratory study on using Slippery-Liquid-Infused-Porous-Surface (SLIPS) for wind turbine icing mitigation. *Renew Energ*. 162:2344–2360.
8 Starostin A, *et al.* 2021. Robust icephobic coating based on the spiky fluorinated Al(2)O(3) particles. *Sci Rep*. 11:5394.
9 Meuler AJ, *et al.* 2010. Relationships between water wettability and ice adhesion. *ACS Appl Mater Interfaces*. 2:3100–3110.
10 Yang S, *et al.* 2021. Condensation frosting and passive anti-frosting. *Cell Rep Phys Sci*. 2:100474.
11 Schutzius TM, *et al.* 2015. Physics of icing and rational design of surfaces with extraordinary icephobicity. *Langmuir*. 31: 4807–4821.
12 Zhang S, *et al.* 2017. Bioinspired surfaces with superwettability for anti-icing and ice-phobic application: concept, mechanism, and design. *Small*. 13:1701867.
13 Mishchenko L, *et al.* 2010. Design of ice-free nanostructured surfaces based on repulsion of impacting water droplets. *ACS Nano*. 4:7699–7707.
14 Guo P, *et al.* 2012. Icephobic/anti-icing properties of micro/nano-structured surfaces. *Adv Mater*. 24:2642–2648.
15 Jin S, Liu J, Lv J, Wu S, Wang SJ. 2018. Interfacial materials for anti-icing: beyond superhydrophobic surfaces. *Chem Asian J*. 13: 1406–1414.

16 Li Q, Guo ZG. 2018. Fundamentals of icing and common strategies for designing biomimetic anti-icing surfaces. *J Mater Chem A*. 6:13549–13581.
17 Stone HA. 2012. Ice-phobic surfaces that are wet. *ACS Nano*. 6: 6536–6540.
18 Lee SH, *et al*. 2018. Tunable multimodal drop bouncing dynamics and anti-icing performance of a magnetically responsive hair array. *ACS Nano*. 12:10693–10702.
19 Guo H, *et al*. 2020. A sunlight-responsive and robust anti-icing/deicing coating based on the amphiphilic materials. *Chem Eng J*. 402:126161.
20 Zhu X, *et al*. 2018. Digital resonant laser printing: bridging nanophotonic science and consumer products. *Nano Today*. 19:7–10.
21 Zhu S, *et al*. 2020. High performance bubble manipulation on ferrofluid-infused laser-ablated microstructured surfaces. *Nano Lett*. 20:5513–5521.
22 Wu C, *et al*. 2020. Highly efficient solar anti-icing/deicing via a hierarchical structured surface. *Mater Horiz*. 7:2097–2104.
23 Wang Z, *et al*. 2021. Temperature self-regulating electrothermal pseudo-slippery surface for anti-icing. *Chem Eng J*. 422:130110.
24 Cheng Y, *et al*. 2021. Rapid and persistent suction condensation on hydrophilic surfaces for high-efficiency water collection. *Nano Lett*. 21:7411–7418.
25 Xu J, Xiu S, Lian Z, Yu H, Cao J. 2022. Bioinspired materials for droplet manipulation: principles, methods and applications. *Droplet*. 1:11–37.
26 Wong TS, *et al*. 2011. Bioinspired self-repairing slippery surfaces with pressure-stable omniphobicity. *Nature*. 477:443–447.
27 Huang YF, *et al*. 2007. Improved broadband and quasi-omnidirectional anti-reflection properties with biomimetic silicon nanostructures. *Nat Nanotechnol*. 2:770–774.
28 Feng L, *et al*. 2002. Super-hydrophobic surfaces: from natural to artificial. *Adv Mater*. 14:1857–1860.
29 Liu K, Yao X, Jiang L. 2010. Recent developments in bio-inspired special wettability. *Chem Soc Rev*. 39:3240–3255.
30 Bhushan B. 2012. Bioinspired structured surfaces. *Langmuir*. 28: 1698–1714.
31 Wong WSY, Hauer L, Cziko PA, Meister K. 2022. Cryofouling avoidance in the Antarctic scallop *Adamussium colbecki*. *Commun Biol*. 5:83.
32 Wu XH, Shen YZ, Zheng SL, Hu ZT, Chen Z. 2020. Clarifying the correlation of ice adhesion strength with water wettability and surface characteristics. *Langmuir*. 36:12190–12201.
33 Xie M, *et al*. 2022. Underwater unidirectional cellular fluidics. *ACS Appl Mater Interfaces*. 14:9891–9898.
34 Zhan Z, *et al*. 2021. 3D Printed ultra-fast photothermal responsive shape memory hydrogel for microrobots. *Int J Extreme Manuf*. 4: 015302.
35 Zhang Y, *et al*. 2022. Ultra-fast programmable human-machine interface enabled by 3D printed degradable conductive hydrogel. *Mater Today Phys*. 27:100794.
36 Zhao J, *et al*. 2022. Two-dimensional ultrathin networked CoP derived from Co(OH)2 as efficient electrocatalyst for hydrogen evolution. *Adv Compos Hybrid Mater*. 5:2421–2428.
37 Rother M, *et al*. 2015. Self-sealing and puncture resistant breathable membranes for water-evaporation applications. *Adv Mater*. 27:6620–6624.
38 Lei M, *et al*. 2022. Breathable and waterproof electronic skin with three-dimensional architecture for pressure and strain sensing in nonoverlapping mode. *ACS Nano*. 16:12620–12634.
39 Lv J, Song Y, Jiang L, Wang J. 2014. Bio-inspired strategies for anti-icing. *ACS Nano*. 8:3152–3169.
40 Sun JY, Bhushan B. 2012. Structure and mechanical properties of beetle wings: a review. *RSC Adv*. 2:12606–12623.
41 Lefevre B, *et al*. 2004. Intrusion and extrusion of water in hydrophobic mesopores. *J Chem Phys*. 120:4927–4938.
42 Xiao R, Enright R, Wang ENJL. 2010. Prediction and optimization of liquid propagation in micropillar arrays. *Langmuir*. 26: 15070–15075.
43 Khattab IS, Bandarkar F, Fakhree MAA, Jouyban A. 2012. Density, viscosity, and surface tension of water plus ethanol mixtures from 293 to 323K. *Korean J Chem Eng*. 29:812–817.
44 Pan YY, Patil A, Guo P, Zhou C. 2017. A novel projection based electro-stereolithography (PES) process for production of 3D polymer-particle composite objects. *Rapid Prototyping J*. 23: 236–245.
45 Yin Q, *et al*. 2021. 3D-printed bioinspired cassie-baxter wettability for controllable microdroplet manipulation. *ACS Appl Mater Interfaces*. 13:1979–1987.